CO_2 hydrogenation to lower olefins on a high surface area K-promoted bulk Fe-catalyst

Carlo Giorgio Visconti [a,*], Michela Martinelli [a], Leonardo Falbo [a], Antonia Infantes-Molina [a,b], Luca Lietti [a,*], Pio Forzatti [a], Gaetano Iaquaniello [c], Emma Palo [c], Barbara Picutti [d], Fabio Brignoli [d]

[a] Politecnico di Milano, Dipartimento di Energia, Via la Masa, 34, 20156 Milan Italy
[b] Universidad de Málaga, Departamento de Química Inorgánica, Cristalografía y Mineralogía, Facultad de Ciencias, Campus de Teatinos, 29071 Málaga Spain
[c] KT- Kinetics Technologies SpA, Maire Tecnimont Group, Viale Castello della Magliana, 75, 00148 Rome Italy
[d] Tecnimont SpA, Maire Tecnimont Group, Via Gaetano de Castillia, 6/A, 20124 Milan Italy

A high surface area K-promoted iron-based catalyst is prepared by thermal decomposition of ammonium glycolate complexes, followed by impregnation with an aqueous solution of potassium carbonate, drying and calcination. It is found that the duration of the calcination has a dramatic effect on the textural and structural properties of the obtained material, as well as on the iron oxidation state. Fast calcinations allow to synthetize materials isostructural with Fe3O4/□-Fe2O3 that, after a carburization treatment with CO/H2 mixtures, are highly active in the CO2 hydrogenation to lower (C2–C4) olefins at mild process conditions (300 ◦C and 5 barg). Interestingly, the decrease of the operating pressure leads to a shift from the "hydrocarbon synthesis" regime to reverse water gas shift regime. The selectivity to lower olefins is instead maximised at mild process conditions due to the moderate chain growth probability and the slow rate of olefin secondary hydrogenations, which dominate at higher pressure and temperatures, respec-tively. The former process is activated by type II catalytic sites (iron carbides), while the latter occurs on type III catalytic sites (Fe0). Type I catalytic sites also exist (Fe3O4) and are responsible for the RWGS activity of the catalyst. Collected data suggest that CO is the primary product of CO2 hydrogenation, while hydrocarbons are formed via CO hydrogenation, following a Fischer-Tropsch type mechanism. Eventu-ally, the performances of the prepared catalyst are compared with those of K-promoted reference model samples based on commercial □-Fe2O3 and Fe3O4 powders. It is found that, due to a better carburiza-tion and the higher surface area, the catalyst prepared by fast decomposition of ammonium glycolate complexes is more active than the reference materials in terms of both CO2 conversion and C2–C4 olefins selectivity.

Keywords: CO_2 hydrogenation, Synthesis of C_2–C_4 olefins, Iron based catalyst, Iron carbides, Potassium promoter, CO_2 capture and utilization CCU

1. Introduction

Considering the estimated dramatic effects of the green-house gases on climate, the reduction of CO_2 emissions from all anthropogenic processes has become one of the key-challenges of the 21st century. Among the alternatives under consideration to achieve such target, researchers are focusing on the reutilization of CO_2 (CCU, Carbon Capture and Utilization) to make added-value products such as fuels and chemicals [1–7]. This opens new opportunities of exploring, developing and applying new concepts in heterogeneous catalysis.

CO_2 is an optimal chemical feedstock: it is abundant, non-toxic and renewable. However, it is thermodynamically stable. Accordingly, its conversion requires high external energy inputs, highly reactive co-reactants and very active and selective catalysts. As a result, the current use of CO_2 as a raw material is only limited to a few industrial processes such as the syntheses of urea and its derivatives, salicylic acid and polycarbonates. Nevertheless, many other promising reactions involving CO_2 as reactant have been reported [1–7]. Among them, the catalytic hydrogenation of CO_2 has been shown to be a versatile route to synthetize valuable

Article history:
Received 19 April 2016
Received in revised form 4 July 2016
Accepted 25 July 2016
Available online 26 July 2016

* Corresponding authors.
E-mail addresses: carlo.visconti@polimi.it (C.G. Visconti), luca.lietti@polimi.it (L. Lietti).

Published Journal Article available at: http://dx.doi.org/10.1016/j.apcatb.2016.07.047

molecules such as methanol, higher alcohols, formic acid, formaldehyde, methane and C_{2+} hydrocarbons. In this regard, it has been noted that even if CO_2 conversion into hydrocarbons requires much more hydrogen (per mole of converted CO_2) than the formation of oxygenates, such route is very appealing as the obtained products have a wider market (fuels) or a higher added value (chemicals) [3].

Hydrocarbons in the fuel range can be obtained *via* a methanol-mediated process or *via* a modified Fischer-Tropsch synthesis (FTS) [1–3]. In the methanol-mediated approach, CO_2 is first converted to methanol, and this latter is converted to hydrocarbons through a methanol-to-gasoline (MTG) process. High cost and catalyst deactivation are the major drawbacks of MTG technologies. At variance, in the case of modified FTS, CO_2 is directly hydrogenated to hydrocarbons [8,9]. The major issue in this case is how to prevent high selectivity to methane and light saturated hydrocarbons [8–11].

Another possible route to exploit CO_2 is its hydrogenation to high add-value chemicals such as lower (C_2–C_4) olefins. These latter molecules are the building blocks of the chemical industry with the largest production volume, and the constantly growing demand of these species, which has caused the global production capacity to double over the past 15 years, asks for new synthesis processes based on low-cost feedstock [12]. Numerous processes have been proposed so far to produce low cost lower olefins. Among them, the dehydrogenation of lower paraffins [13], the two step process from methane [14] and the conversion from synthesis gas either directly (FTO, Fischer-Tropsch to olefins) [10,15–18] or via methanol (MTO, methanol to olefins) [19,20] have been widely studied. On the contrary, only few studies have been recently reported on the selective hydrogenation of CO_2 to C_2–C_4 olefins [5,16,21–27], a one-pot process which is often described as the combination of two consecutive reactions occurring in the same reactor, i.e. the reverse-water-gas-shift reaction (Eq. (1)) and the CO hydrogenation to olefins (Eq. (2)):

$$CO_2 + H_2 \leftrightarrow CO + H_2O \quad (1)$$

$$nCO + 2nH_2 \rightarrow C_nH_{2n} + nH_2O \quad (2)$$

In some cases, the co-presence of the direct hydrogenation of CO_2 to olefins has been also proposed [28].

Among VIII group metals, which are known to be active in CO hydrogenation, iron based catalysts are interesting candidates for the production of olefins from CO_2. Indeed, iron based catalysts are active for both the water-gas-shift reaction and the Fischer-Tropsch synthesis. Also, at least during the Fischer-Tropsch synthesis from CO, high olefins content can be achieved at temperatures higher than 300 °C, which are required to drive the product selectivity towards short chain hydrocarbons [29]. At these conditions, in fact, iron based catalysts have low activity for the undesired reactions including CO methanation and olefins hydrogenation [30]; however, promoters must be added to the catalyst in order to achieve high selectivity to olefins.

Potassium has been extensively studied as promoter of Fe-based Fischer-Tropsch catalysts and, more recently, of Fe-based catalyst for CO_2 hydrogenation. It has been shown that it favors CO and CO_2 adsorption, increases the chain growth probability and enhances the production of olefins [9,21,22,31,32]. However, its effects on the product selectivity and on the catalyst activity have been found to be strongly dependent on its concentration and on the reaction conditions, including the nature of the reacting mixture, containing CO or CO_2. For example, during CO_2 hydrogenation, You et al. [23] observed that C_2–C_4 olefin selectivity increases upon addition of potassium and achieves a value of 34% for a 5 wt.% K-promoted iron-based catalyst (340 °C, 20 bar, $H_2/CO_2 = 3$, 1200 $Ncm^3/h/g_{cat}$). Even higher C_2–C_4 olefin selectivity (49%) was obtained by Zhang et al. [26] on a Fe_2O_3 catalyst with 4.5 wt.% potassium (320 °C, 5 bar, $H_2/CO_2 = 3$, 1000 $Ncm^3/h/g_{cat}$). Xu et al. [33], on the contrary, reported a selectivity of 56% on a 10 wt.% K- and MnO promoted Fe/silicalite-2 catalyst (347 °C, 20 bar, $H_2/CO_2 = 3$, 1200 $Ncm^3/h/g_{cat}$). Accordingly, an optimization work is required to design and synthetize K-promoted iron based catalysts particularly effective for CO_2 hydrogenation to lower olefins.

It has been reported that high olefin selectivity can be achieved in CO_x hydrogenation when iron oxide is effectively converted to iron carbides [34,35]. In this regard, Soled et al. [34] proposed a method to synthetize Fe-based catalysts based on the thermal decomposition of ammonium glycolate complexes formed by drying a solution of iron nitrate, glycolic acid and ammonium hydroxide. It has been claimed that the thermal decomposition of such complexes brings to low density amorphous solid which can be converted by proper treatments to a high surface area oxide with small particle size [35], isostructural with Fe_3O_4 (spinel structure), and easily convertible into Hägg carbide (χ-Fe_5C_2) [34]. This active phase, once promoted with alkali, has been claimed to have very interesting performances in the synthesis of C_2–C_{20} olefins. Indeed, CO_2 conversion and the olefins content in C_2–C_4 fraction are reported to be superior to those obtained by testing a conventional precipitated iron catalyst (Fe/Cu/K/Si) at the same process conditions [34]. Unfortunately, however, only a few activity data are reported in the aforementioned patent [34], and the catalyst synthesis procedure is missing of some key information. Also a comparison of the performances of the catalyst prepared according to the method claimed in [31] and catalytic materials prepared by a more conventional incipient wetness impregnation of precipitated iron oxides is missing.

The aim of this work is to gain further insights on the performances of catalysts similar to those claimed in [34]. To the scope, K-promoted bulk iron catalysts have been prepared according to the procedure reported in [34]. A detailed investigation on the effects of the calcination treatment on the properties of the obtained materials has been carried out, with a particular attention devoted to the iron oxidation state, the textural properties and the surface morphology. The catalyst with the highest surface area and the highest content of an iron-phase isostructural with Fe_3O_4 (spinel structure) has been tested in CO_2 hydrogenation at different process conditions. The catalytic consequences of the key-parameters involving in the catalyst synthesis procedure have been investigated. Similarly, the effect of the process conditions (temperature, pressure, space velocity and H_2/CO_2 feed ratio) on the catalyst activity and selectivity have been studied. Finally, the performances of the prepared catalyst have been compared to those of K-promoted reference samples prepared from commercial α-Fe_2O_3 and Fe_3O_4 samples.

2. Experimental

2.1. Catalyst preparation

Following the procedure proposed in [34], iron catalysts have been prepared by evaporating to dryness an aqueous solution containing a soluble iron salt and a α-hydroxy aliphatic carboxylic acid and then heating at high temperature the obtained amorphous residue.

More specifically, an iron solution has been prepared by dissolving iron(III) nitrate nonahydrate (Sigma Aldrich, >98%) in deionized water (57.9 wt.%), while a α-hydroxy aliphatic acid solution has been prepared by dissolving glycolic acid (Sigma Aldrich, 99%) in deionized water (85 wt.%), adding ammonium hydroxide (Sigma Aldrich, 28–30% NH_3 basis) so to reach a pH value of 7. Then, the ammonium glycolate solution has been added to the iron solution operating under stirring at room temperature, with a molar ratio glycolic acid to iron of 1.073. The resulting solution has been dried

in a rotary evaporator at 60 °C for 3 h under vacuum, and then the solid residue has been dried in static air at 45 °C overnight. This procedure has been done with particular care to avoid the fast and uncontrolled decomposition of ammonium nitrate that can be formed. The obtained solid (named "**dry precursor**") has been eventually crushed and calcined in static air at 350 °C.

Different durations of the calcination process, between 15 and 60 min, have been explored in order to identify an effective procedure to decompose the organic compounds and form the desired spinel structure isostructural with Fe_3O_4 with a high surface area. The obtained samples ("calcined precursors") have been indicated as "**FeX**", where X is the calcination time in minutes.

The calcined precursor with the higher surface area and the greater content of a phase isostructural with Fe_3O_4 has been promoted with potassium (K/Fe = 0.02 molar ratio) by single-step incipient wetness impregnation (IWI), using an aqueous solution of K_2CO_3 (Sigma Aldrich, ≥99%). After impregnation the sample has been dried overnight at 100 °C. The obtained sample has been named "**K-FeX**".

Other two catalysts have been prepared for comparison purposes by IWI of reference model samples of α-Fe_2O_3 (Sigma Aldrich, >99% trace metal basis) and Fe_3O_4 (Sigma Aldrich, 95% trace metal basis), using an aqueous solution of potassium carbonate (K/Fe = 0.02 molar ratio). The obtained samples have been named "**K-α-Fe_2O_3**" and "**K-Fe_3O_4**", respectively.

2.2. Catalyst characterization

The thermal decomposition of the dry precursor during heat treatment has been investigated by thermogravimetric/thermal analysis (TG/DTA) with an Exstar 6000 instrument from Seiko Instruments. In a typical run the sample has been heated in synthetic air (~300 Nl/h/g_{cat}) from ambient temperature to 800 °C at 5 °C/min.

Temperature programmed decomposition in oxygen (O_2-TPD) of dry-precursor has been also carried out by using a stream of 2 vol.% O_2 in He (Sapio) at 100 Nl/h/g_{cat} and by heating the sample from ambient temperature to 500 °C at 10 °C/min. The gaseous products of decomposition have been analysed by using an on-line quadrupole mass-spectrometer (Pfeiffer Omnistar). The mass-to-charge ratios (m/z) used to identify the reaction products are 18 (H_2O), 28 (CO), 30 (NO), 32 (O_2), 44 (CO_2) and 45 (COOH).

The textural properties of the synthetized samples have been determined by N_2 adsorption-desorption isotherms measured at −196 °C by using a Micromeritics Tristar 3000 instrument. Prior to the analysis the samples have been evacuated at 120 °C for 3 h.

Powder X-ray diffraction measurements have been carried out using a D8 Advance Bruker diffractometer and Cu-Kα radiation (λ = 1.54 Å). A scan rate of 0.05° per step and a scan time of 12.5 s^{-1} over a 2θ range of 20–70° have been adopted. The average crystallite size has been calculated by using the Scherrer equation on the peaks at 2θ = 33.3° (α-Fe_2O_3) and 30.4° (γ-Fe_2O_3/Fe_3O_4).

Catalyst reducibility has been estimated by temperature programmed reduction in H_2 (H_2-TPR), using a Thermo Scientific TPDRO 1100 instrument. In a typical test the powdered catalyst has been placed in a quartz reactor and, after a pre-treatment in flowing He (300 Nl/h/g_{cat}, Rivoira) carried out by heating from ambient temperature to 350 °C at a rate of 10 °C/min, has been cooled down to ambient temperature leaving He flow open. Then, the flow has been switched to 20 vol.% H_2 in Ar (Sapio) at 120 Nl/h/g_{cat} and the reactor temperature has been increased to 1000 °C at 15 °C/min. Hydrogen consumption has been monitored by a thermal conductivity detector (TCD) placed downstream the reactor, after a soda lime trap removing water formed in the reduction process. TCD response factor of H_2 has been estimated by calibration with CuO standard (Aldrich, 99.999% trace metal basis).

Table 1
Process conditions investigated with the K-Fe15 sample.

Condition	Temperature [°C]	Pressure[barg]	GHSV [$Ncm^3/h/g_{cat}$]	H_2/CO_2 [v/v]
#1	270	5	2700	3
#2	300	5	2700	3
#3	300	0	2700	3
#4	300	10	2700	3
#5	300	5	5400	3
#6	300	5	10800	3
#7	300	5	16000	3
#8	300	5	2700	1

The surface nature of the dry precursor, the fresh catalysts and the used K-Fe15 sample has been analysed by X-Ray Photoelectron Spectroscopy (XPS). To the scope, a 5000 Versaprobe II spectrometer with a monochromatic Al-Kα radiation has been used. Spectra have been recorded in the constant pass energy mode at 29.35 eV, using a 720 μm diameter analysis area. Charge referencing has been measured against adventitious carbon (C 1s at 284.8 eV). A SmartSoft VersaProbe software package has been used for acquisition and data analysis. A Shirley-type background has been subtracted from the signals.

TEM images of the K-Fe15 sample have been collected by HRTEM using a TEM/STEM FEI Talos F200X microscope provided with a DF1 detector, a high brightness field emission gun (XFEG) and working at 200 kV. To the scope, the sample has been suspended in ethanol and a drop of this suspension has been put on a lacey carbon-coated Cu grid.

2.3. Catalyst testing

Activity tests have been carried out in a lab-scale plant equipped with a fixed-bed reactor, placed into an electric furnace. More details on the experimental rig and on the process analytics can be found elsewhere [9]. We recall here that the adopted set-up allows the quantification of the flow rates of C_1–C_9 hydrocarbon species, in addition to CO, CO_2, H_2, N_2 and Ar.

The best K-FeX powdered catalyst (average particle size of 100 μm), diluted with powdered α-Al_2O_3 (1:10 v/v) with the same particle size, has been loaded in the reactor and activated in situ at 350 °C (heating ramp = 1 °C/min) for 1 h, feeding a H_2/CO/N_2 (31.3/32.0/36.7 v/v) mixture (2700 $Ncm^3/h/g_{cat}$) at atmospheric pressure. Then the reactor has been cooled down to 270 °C, the mixture H_2/CO_2/Ar (73.0/25.0/2.0 v/v) has been admitted to the reactor and the pressure has been slowly raised to 5 barg. The catalyst has been operated in this condition (condition #1, Table 1) for 75 h until steady state conditions for both CO_2 conversion and product selectivity have been reached. Then, the effects of temperature (270–300 °C), pressure (0–10 barg), space velocity (2700–16000 $Ncm^3/h/g_{cat}$) and H_2/CO_2 ratios (1–3 v/v) (conditions #2–#8) have been investigated.

In order to compare the performances of K-α-Fe_2O_3 and K-Fe_3O_4 catalysts with those of the best K-FeX sample, the same flow rate per unit of BET area (41 $Ncm^3/h/m^2_{cat}$) has been used, by using the same reactor inlet flow rate and changing the catalyst loading in the reactor accordingly. Also, the same activation procedure has been used for the three samples.

Among the reaction products, H_2O, CO, C_1–C_9 paraffins, C_2–C_9 olefins, and minor amounts (accounting for less than 5% of converted CO_2) of C_1–C_5 alcohols, C_3–C_5 ketones and C_2–C_5 carboxylic acids were identified, but only CO, C_1–C_9 paraffins and C_2–C_9 olefins were quantified because of the limits of the adopted set-up. Carbon

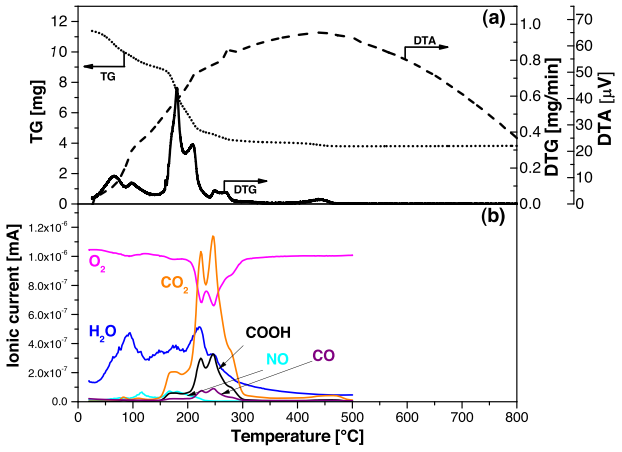

Fig. 1. (a) TG/DTA in air and (b) O_2-TPD for the "dry precursor".

selectivities (S_i, Eq. (3)) of these latter species have been calculated according to the following equation:

$$S_i = \frac{F_i^{OUT} \cdot n_i}{\sum_{i=1}^{9} F_i^{OUT} \cdot n_i} \quad (3)$$

where F_i^{OUT} is the molar productivity of the i species (CO and C_1–C_9 hydrocarbons) and n_i is the carbon number of this species.

3. Results and discussion

3.1. Catalysts characterization

3.1.1. Dry precursor

The results of TG/DTA in air and O_2-TPD measurements, carried out to investigate the phenomena taking place during the thermal decomposition of the dry precursor, are shown in Fig. 1. As clearly visible from TG and DTG profiles (Fig. 1(a)) two main phenomena occur, one in the 25–140 °C temperature range, characterized by a weight loss of 23%, the other in the 140–300 °C temperature range, characterized by a weight loss of 50%. DTA profile shows that no one of these phenomena is associated to strongly exothermic or endothermic processes.

The product evolution observed during O_2-TPD experiment (Fig. 1(b)) is similar to that of DTG, although the observed phenomena are shifted to slightly higher temperatures because of the different heating rate (10 °C/min vs. 5 °C/min) adopted in the two experiments. At temperatures below 140 °C the H_2O signal increases from ambient temperature until a maximum, which is reached at 95 °C, indicating that the weight loss of 23% observed during the TG/DTA experiment is due to the sample dehydration. As expected, such phenomenon does not cause any consumption of O_2. Small amount of NO is also detected, associated to the decomposition of residual iron nitrates used to prepare the catalyst.

By increasing the temperature from 140 °C to 300 °C, H_2O shows a further desorption, along with CO_2, CO and COOH showing similar trends with maxima detected at 175, 225 and 247 °C. Also, the consumption of oxygen is observed in correspondence to these three maxima. This result suggests that iron complexes undergo oxidative decomposition in this temperature range, leading to a 50% weight loss.

According to the literature [35–39], in presence of α-hydroxy carboxylic acids, the Fe(III) nitrate salt forms a glycolate iron complex ($Fe(C_2O_3H)_3{\cdot}xH_2O$), whose decomposition takes place in the 150–300 °C temperature range [38]. At first, an endothermic decomposition occurs, corresponding to the release of gaseous organic compounds which act as reductants on Fe(III) species, transforming a part of them into Fe(II). This step is followed at higher temperatures by the exothermic combustion of the organic gaseous products. Due to the consumption of the reducing species in the gas phase and the contemporary presence of O_2, at this point Fe(II) species are re-oxidized to Fe(III) species [38].

In our sample, the decomposition of $Fe(C_2O_3H)_3{\cdot}xH_2O$ complex observed between 225 and 300 °C possibly results in the release of CO, which acts as reductant of Fe(III) species. Accordingly, Fe_3O_4 (magnetite) spinel can be formed. At higher temperatures the presence of O_2 results in the oxidation of Fe(II) to Fe(III), and as a result γ-Fe_2O_3 (maghemite) or α-Fe_2O_3 (hematite) phases are formed, depending on both temperature and duration of calcination [37]. In this regard it is worth noticing that γ-Fe_2O_3 is not stable at temperatures higher than 350 °C, and is transformed in the corundum structure with a closed-packed oxygen lattice (α-Fe_2O_3) [38].

The XPS Fe 2*p* and C 1*s* core level spectra of the dry-precursor are shown in Fig. 2, while the atomic composition of its surface is given in Table 2. The analysis of the Fe 2*p* core level spectrum is quite complex due to spin-orbit splitting, multiple oxidation states and satellite structures, which complicate the determination of the relative concentration of Fe(II) and Fe(III). Nevertheless, the presence of Fe $2p_{3/2}$ and Fe $2p_{1/2}$ contributions coming from the spin-orbit splitting and the position of the most intense peaks at binding energy values 710.5–711.5 eV and 724.2–725.1 eV, respectively, suggest that Fe_3O_4 is likely to be the dominant oxide on the catalyst surface [40–42]. In addition to these species, as clearly shown by the atomic composition of the surface (Table 2), organic species (glycolate iron complexes), as well as N-containing compounds (ammonium complexes, nitrates), are abundant on the catalyst surface.

Table 2
Surface compositions (at.%) of dry precursor, Fe15, Fe30, Fe60 and used K-Fe15 catalyst samples.

	C	O	Fe	N
Dry precursor	42.9	45.5	8.5	3.1
Fe15	19.6	50.7	29.7	–
Fe30	18.2	56.7	25.1	–
Fe60	19.9	59.9	20.2	–
Used K-Fe15	81.2	14.3	4.5	–

Table 3
Textual properties of Fe15, Fe30 and Fe60 samples and of the reference model samples (α-Fe_2O_3 and Fe_3O_4).

	Surface area [m^2/g]	Pore volume [cm^3/g]	Average pore diameter [nm]
Fe15	66.6	0.13	6.2
Fe30	46.2	0.13	8.7
Fe60	23.3	0.09	14.3
α-Fe_2O_3	4.6	–	–
Fe_3O_4	5.2	–	–

3.1.2. Calcined catalysts (Fe15, Fe30 and Fe60 samples)

The morphological properties of the catalysts prepared by calcining the dry precursor for 15, 30 and 60 min (Fe15, Fe30 and Fe60, respectively) are reported in Table 3. The surface area of Fe15 sample is 67 m^2/g, a high value for a bulk Fe-oxide prepared without adding any structural promoter or other heteroatoms, for which surface areas ranging from 20 to 50 m^2/g are usually reported in the literature [43–47]. Upon increasing the duration of the calcination from 15 to 60 min, the surface area drops from 67 to 23 m^2/g, while the average pore diameter increases from 6 to 14 nm.

The calcination time also affects the textural properties of the catalysts. The XRD patterns, shown in Fig. 3, point out that Fe_3O_4/γ-Fe_2O_3 are the main crystalline phases for the Fe15 sample and only a minor diffraction signal appears at $2\theta = 33.2°$, assigned to α-Fe_2O_3. Unfortunately, it is not possible to distinguish whether magnetite

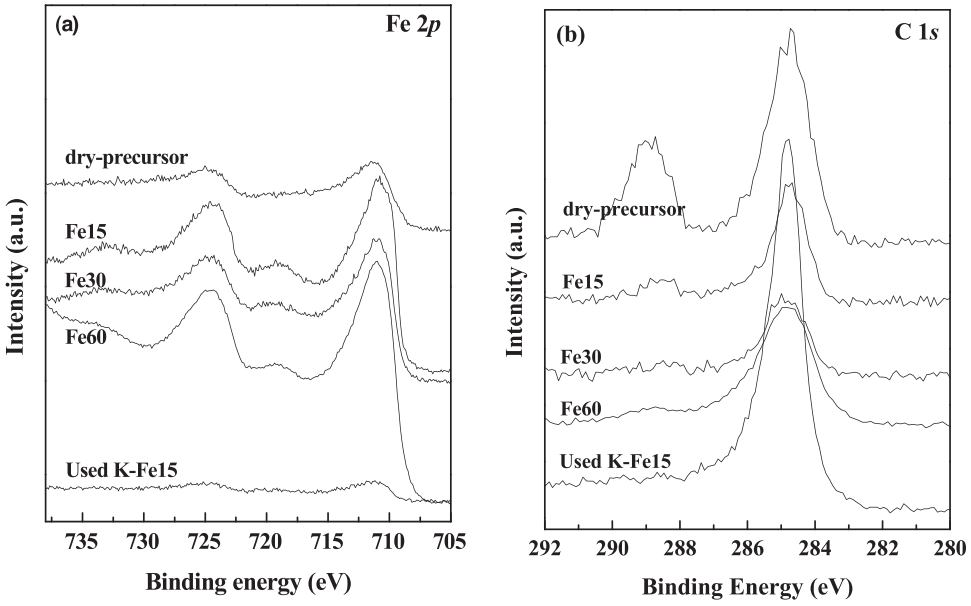

Fig. 2. XPS spectra. (a) Fe 2*p* and (b) C 1*s* core levels.

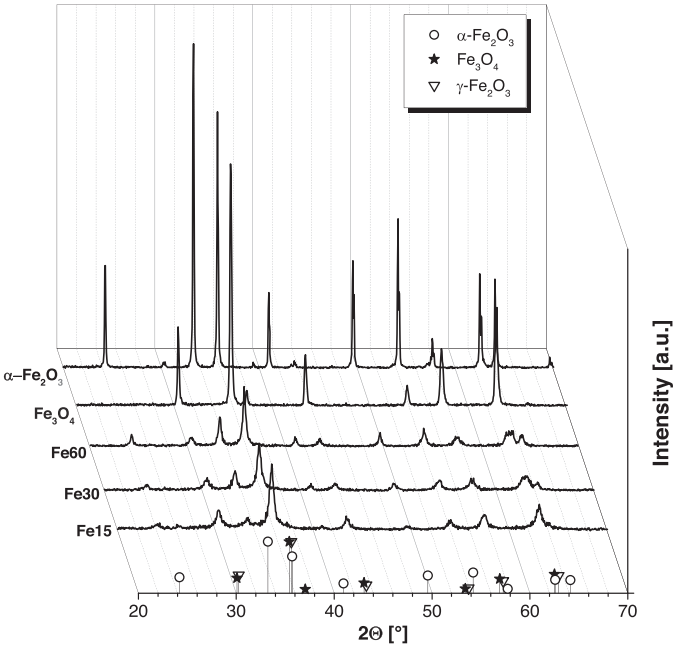

Fig. 3. XRD patterns of Fe15, Fe30, Fe60, Fe_3O_4 and α-Fe_2O_3 samples.

or maghemite (or a mixture of them) is present in our sample. Indeed, even though maghemite should exhibit few extra peaks at 23.8° (2 1 0) and at 26.1° (2 1 1), which are often used to distinguish it from magnetite [48], in our case (microcrystalline/amorphous sample) the intensities of these peaks are too weak to draw a final conclusion.

By prolonging the calcination time the Fe_3O_4/γ-Fe_2O_3 phases are progressively converted into α-Fe_2O_3, as demonstrated by the increase of the ratio between the peaks at $2\theta = 33.2°$ and 35.7°. As a result the XRD pattern of Fe60 sample is mostly characterized by the presence of the diffraction peaks typical of the α-Fe_2O_3 phase.

The average crystal size (D_{cry}) of Fe_3O_4/γ-Fe_2O_3 and α-Fe_2O_3 in the Fe15, Fe30 and Fe60 samples are reported in Table 4. The average crystal size calculated from the XRD pathways grows from 13 to 17 nm in the case of γ-Fe_2O_3/Fe_3O_4 phase and from 18 to 24 nm in the case of α-Fe_2O_3 phase. These estimates well correspond to what can be measured through TEM imaging, as pointed out for example in Fig. 4 for the Fe15 sample. It is evident that the iron phase transition is associated to an increase of the crystallite size, especially in the case of hematite phase. These results are in line with literature indications on similar materials. In particu-

Table 4
Average crystallite size of Fe15, Fe30 and Fe60 samples estimated with Scherrer equation.

	Phase	2θ	D_{cry} [nm]
Fe15	α-Fe_2O_3	–	–
	γ-Fe_2O_3/Fe_3O_4	30.25	13.0
Fe30	α-Fe_2O_3	33.29	18.2
	γ-Fe_2O_3/Fe_3O_4	30.41	14.2
Fe60	α-Fe_2O_3	33.39	23.9
	γ-Fe_2O_3/Fe_3O_4	30.51	16.6

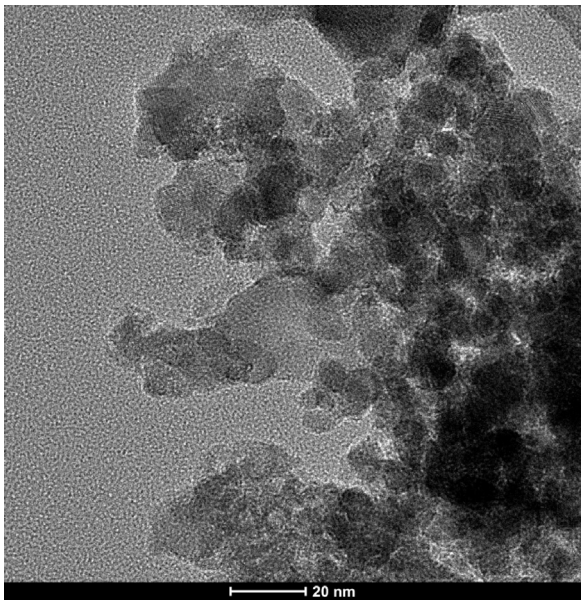

Fig. 4. TEM image of Fe15 sample.

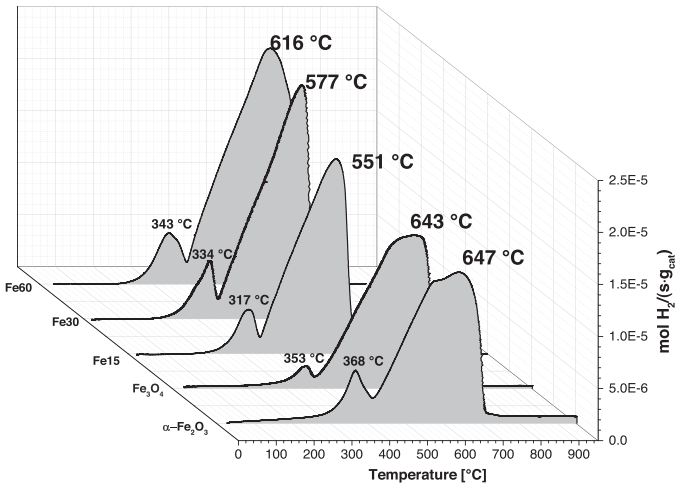

Fig. 5. H_2-TPR profiles of Fe15, Fe30, Fe60, α-Fe_2O_3 and Fe_3O_4 samples.

lar Mendili et al. [49] reported that maghemite nanoparticles are obtained at temperature lower than 300 °C. At higher temperature the germination of the hematite phase at maghemite nanoparticle boundary causes the increase of the crystallite size. The hematite phase grows toward the core of the nanoparticle and slowly induces a phase change (γ-Fe_2O_3/α-Fe_2O_3) at temperatures between 350 °C and 400 °C [49]. This type of polymorphic transformation is also reported for the transition of spinel (γ) to corundum (α) phase in Al_2O_3 [49].

The H_2 consumption profiles during H_2-TPR experiments (Fig. 5) show two major reduction peaks for the three FeX samples, centred in the ranges 300–400 °C and 400–700 °C. According to the literature [9,50] the first peak, which accounts for about 10% of the total area under the TPR curve regardless the duration of calcination, is due to the reduction of Fe_2O_3 (maghemite or hematite) to Fe_3O_4 (partial reduction of Fe(III) to Fe(II), Eq. (4)), whereas the second peak, much higher and broader, corresponds to the reduction of Fe_3O_4 to metallic iron (Eq. (5)):

$$3Fe_2O_3 + H_2 \rightarrow 2Fe_3O_4 + H_2O \quad (4)$$

$$Fe_3O_4 + 4H_2 \rightarrow 3Fe + 4H_2O \quad (5)$$

The latter step (Eq. (5)) is expected to be rather complex, because it involves the transformation of a mixture of Fe(III) and Fe(II) to Fe^0, which possibly occurs through the formation of FeO species [51]. This is the reason why the second peak is broad for all the FeX samples we prepared.

Upon increasing the duration of the calcination, the maximum of the first peak shifts to higher temperatures (from 317 to 343 °C) and the same occurs for the second peak, which shifts from 551 °C to 616 °C. The progressive shift at higher temperatures for both the peaks can be explained considering that, upon increasing the duration of the calcination, the surface area of the samples decreases as a consequence of the increased size of the crystallites and the content of Fe(III) species increases at the expenses of Fe(II) species.

The results previously reported are confirmed by XPS spectra shown in Fig. 2, where the contribution at 284.8 eV, present in all samples, is due to adventitious carbon. Both Fe_3O_4 and Fe_2O_3 (possibly in its spinel phase) are present on the surfaces of FeX samples, which are at the same time free of N and poor of C-species (Table 2) as a result of the complete decomposition of the organic species present in the dry precursor. Interestingly, the superficial O/Fe ratio (Table 2) keeps growing upon prolonging the calcination time, in line with a progressive oxidation of Fe_3O_4 to Fe_2O_3 species.

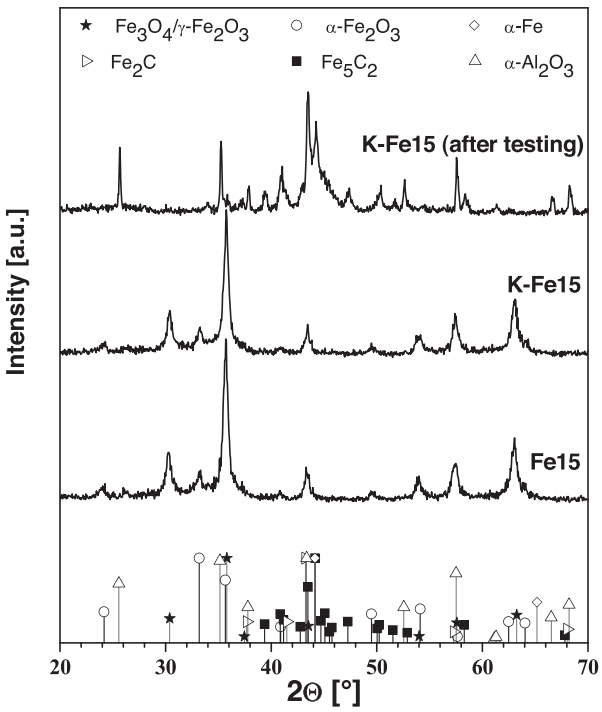

Fig. 6. XRD patterns of Fe15, fresh K-Fe15 and used K-Fe15 samples.

3.1.3. *Reference model samples: α-Fe_2O_3 and Fe_3O_4*

The specific surface areas of commercial α-Fe_2O_3 and Fe_3O_4 samples, given in Table 2, are quite low, being both around 5 m^2/g. The XRD patterns (Fig. 3) show indeed that both materials are very crystalline. As expected, hematite dominates in the α-Fe_2O_3 sample, while magnetite dominates in the Fe_3O_4 sample. Nevertheless impurities of Fe_3O_4 are visible (peak at $2\theta = 30.4°$) in the patters of α-Fe_2O_3 sample.

As in the case of FeX samples, the H_2-TPR profiles of model reference materials (Fig. 5) show two main reduction peaks which are shifted at higher temperature than those of Fe15, Fe30 and Fe60 samples because of the lower surface area of commercial samples. Notably, the presence of two reduction peaks is expected in the case of α-Fe_2O_3 sample because of the occurrence of the two reduction steps (Eq. (4)) and (Eq. (5)) previously discussed, but is unexpected for the Fe_3O_4 sample, which should give a single reduction peak at high temperature. In line with literature indication [52], the presence of a small peak between 300 and 400 °C for the Fe_3O_4 commercial sample is due to the presence of some Fe_2O_3 impurities.

3.2. *Catalytic activity runs*

The catalyst with the highest surface area and with the greatest fraction of a spinel type-structure, namely the Fe15 sample, has been promoted with potassium and then tested in CO_2 hydrogenation to C_2–C_4 olefins after activation at 350 °C with syngas (cf. Section 2.3). The catalytic behaviour of this sample has been compared with that of the reference K-doped Fe_3O_4 and Fe_2O_3 samples. Notably, as shown by comparing the XRD patterns before and after K-impregnation for the Fe15 sample (Fig. 6), the addition of potassium does not change the structural characteristics of the samples regardless its high surface area.

3.2.1. *K-Fe15 sample*

3.2.1.1. Catalyst activation. The specific flow rates (per unit of catalyst surface area) of unconverted reactants (CO, H_2) and of reaction

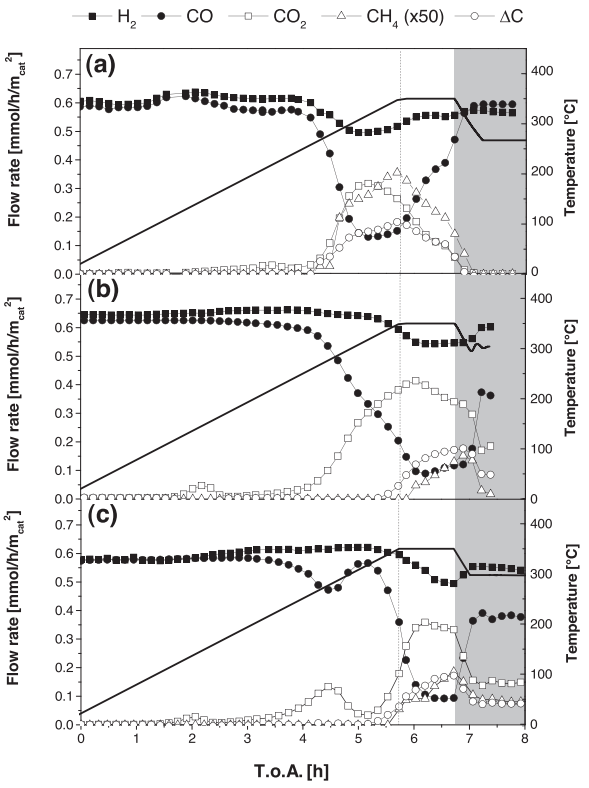

Fig. 7. Specific flow rate during the activation of (a) K-Fe15, (b) K-α-Fe_2O_3, (c) K-Fe_3O_4 catalysts (heating from ambient temperature to 350 °C at 1 °C/min and holding for 1 h, 0 barg, $H_2/CO/N_2$ = 31.3/32.0/36.7 v/v).

products (CH_4, CO_2) measured during the catalyst activation process are shown as a function of time of activation (T.o.A.) in Fig. 7(a).

No relevant CO and H_2 consumptions, nor product formation, are observed until 250 °C. By increasing the temperature further, H_2 and CO react and their specific flow rates decrease until a minimum, which is achieved for both reactants at 325 °C. In correspondence to this consumption, the formation of CO_2 and CH_4 is observed. Nevertheless, the two species show different trends, with CH_4 monotonically growing during the T-ramp, and CO_2 showing a maximum at 325 °C (i.e. in correspondence of the minimum for H_2 and CO). The appearance of CH_4 over 250 °C suggests at this temperature the reduction of some iron oxide species to metallic iron (in line with H_2-TPR profiles shown in Fig. 5) followed by carburization of Fe^0 to catalytic sites active in CO_x hydrogenation [53].

The carbon balance (ΔC), calculated by using Eq. (6), is also plotted versus the time of activation in Fig. 7(a).

$$\Delta C = F_{CO}^{in} - F_{CO}^{out} - F_{CO_2}^{out} - F_{CH_4}^{out} \quad (6)$$

In this equation F_{CO}^{in} is the CO specific (per unit of surface area) flowrate fed to the reactor and F_{CO}^{out}, $F_{CO_2}^{out}$ and $F_{CH_4}^{out}$ are CO, CO_2 and CH_4 specific flowrates leaving the reactor.

As expected, ΔC is nil during the first 4 h of activation, when no CO is consumed, while grows starting at 250 °C, confirming that some carbon is accumulating on the catalyst. Notably, at temperatures above 250 °C, a significant consumption of H_2 is also detected, which is not justified by the small amount of methane formed or by the amount required for a complete iron reduction. This suggests that hydrogen is involved in the formation of surface carbon-containing species (CH_x). The formation of iron carbides is however likely to occur, as suggested by the fact that the catalyst becomes active in CO hydrogenation at temperatures over 250 °C. Unfortunately, our analyses do not allow to estimate the fraction of carbon forming iron carbides and the fraction of carbon deposited as CH_x residue. Indeed, both the presence of CO_2 in the gas phase and the molar ratio between consumed CO and formed CO_2 are consistent with either the deposition of carbon containing species (Eq. (7)) or the formation of iron carbides (here described as Hägg carbide as example, Eq. (8)) [54].

$$2CO + \frac{x}{2}H_2 \rightarrow CH_x + CO_2 \quad (7)$$

$$5Fe^0 + 4CO \rightarrow Fe_5C_2 + 2CO_2 \quad (8)$$

Both the carbon deposition, the methane production and the H_2 and CO consumptions continue during the period in which the temperature is kept constant at 350 °C. However, when the system is cooled to 270 °C, CH_4 and CO_2 specific flow rates drop to zero, as well as the carbon balance and H_2 and CO consumptions. This suggests that reactions Eqs. (7) and (8) are kinetically quenched at these conditions.

3.2.1.2. Catalyst start-up. The evolution of the catalyst performances during the first 75 h under H_2/CO_2 is shown in Fig. 8. CO_2 conversion progressively increases from 16% until a steady state value near 37% is reached in about 45 h. H_2 conversion follows a similar trend by increasing from 9% to about 40%. Notably, while the H_2 conversion is lower than CO_2 conversion in the first 15 h on stream, the situation is opposite at steady state. As a result, at low time on stream (T.o.S.) the H_2/CO_2 usage ratio is about 2 (Fig. 8(a), inset), but progressively increases with T.o.S. reaching a value of 3. These results can be explained by considering that both the RWGS (Eq. (1), H_2/CO_2 usage ratio = 1) and the consecutive synthesis of hydrocarbons from CO (Eq. (2), H_2/CO usage ratio = 2) are taking place on the catalyst, and that the relevance of the two processes changes with time on stream as a consequence of modifications of the active sites.

The analysis of the evolution of the product selectivity with T.o.S. may offer insights on these transformations. Fig. 8(b) shows that CO is the main reaction product at low time on stream (<15 h), but then its selectivity rapidly decreases. Similarly to CO, methane selectivity also decreases with time on stream. As opposite, the selectivity to C_2–C_4 olefins as well as the selectivity to C_{2+} paraffins increase during the first 50 h.

The evolution of olefin to paraffin ratio in the product gives also information on the catalyst active sites. Indeed, it offers insights on the type of sites available on the catalyst, especially in terms of ratio between the number of chain growth sites and the number of the hydrogenation sites [53,55,56]. Our data (Fig. 9) show that the olefin to paraffin ratio has a maximum for the C_3 species, and then linearly decreases with increasing the carbon number. C_2 species are out of trend and this can be explained considering the high reactivity of ethylene with respect secondary hydrogenation reactions [56]. During the first 75 h on stream the olefin/paraffin ratio increases, evolving rapidly during the first 30 h on stream and then evolving more slowly until approaching a pseudo-steady-state level (Fig. 9, inset).

It has been reported that many co-existing active phases are involved in CO hydrogenation on iron-based catalysts, including Fe^0, Fe_3O_4 and iron carbides. The specific catalytic activity of each phase is still debated. Nevertheless, it is generally accepted that at least two different active sites exist on the catalyst surface. Type I sites, usually identified with Fe_3O_4, are considered the most active for the WGS/RWGS reactions [30,56], as well as for the reactions bringing to the formation of oxygenated products [57]. Type II sites, usually identified as iron carbides, are considered active for CO activation and C–C bond formation (chain growth) [53,58–60]. In this picture, α-Fe is often considered inactive during CO_x hydrogenation [60]. However, Shultz [55] observed that when some metallic iron is present on the catalyst surface, appreciable olefins hydrogenation

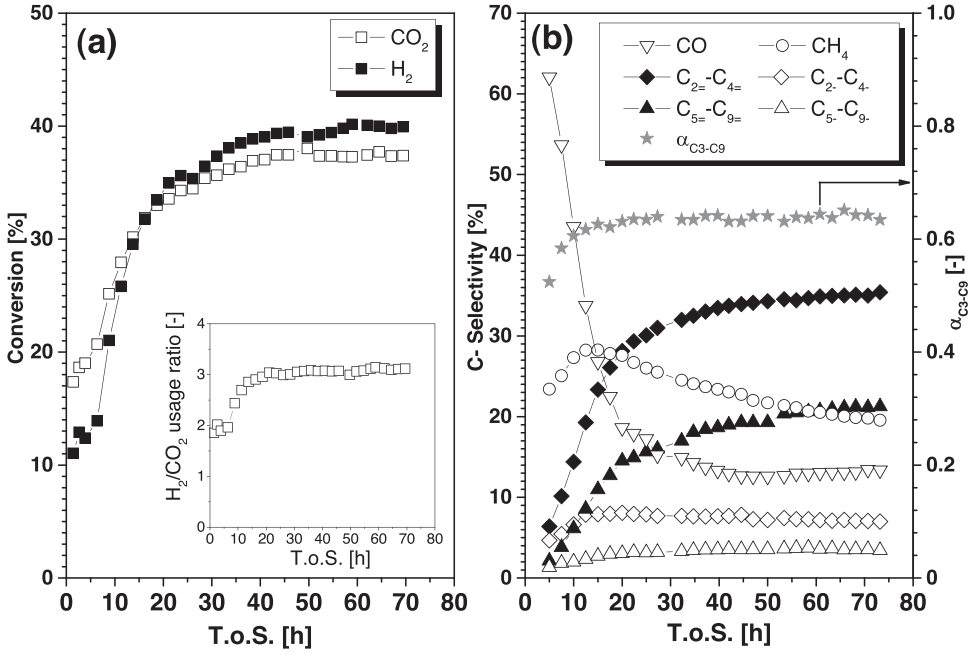

Fig. 8. Evolution with T.o.S. of (a) H_2 and CO_2 conversion and (b) C-selectivity and chain growth probability for K-Fe15 sample (process conditions: T = 270 °C, P = 5 barg, GHSV = 2700 $Ncm^3/h/g_{cat}$, H_2/CO_2 = 3 v/v). Fig. 8(a) inset: evolution with T.o.S. of the H_2/CO_2 usage ratio.

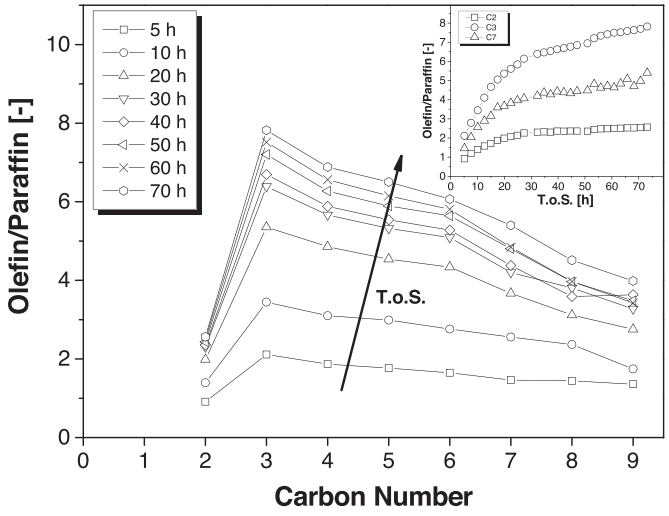

Fig. 9. Evolution of the Olefin/Paraffin ratio with T.o.S. for K-Fe15 catalyst during the first 75 h on stream. Inset: evolution with T.o.S. of the Olefin/Paraffin ratio for the C_2, C_3, C_7 species. Process conditions as in Fig. 8.

activity appears, thus suggesting the existence of an additional site, type III, which is responsible for the olefins secondary reactions. It is also reported that type I and type III sites may evolve to type II sites with time on stream during the so-called "catalyst reconstruction" [55].

Our results are in line with the fact that types I, II and III sites are also relevant during CO_2 hydrogenation and that even in the presence of CO_2/H_2 mixture in the feed type I and III sites can evolve in type II site. Indeed: (i) the increase of CO_2 and H_2 conversion with T.o.S. suggests that the number of type II sites (CO activation) is increasing with T.o.S.; (ii) the decrease of CO selectivity, the increase of hydrocarbon selectivity and the consequent increase of H_2/CO_2 usage ratio suggest that type I sites (WGS/RWGS sites) are decreasing and/or type II sites (chain growth) are increasing with T.o.S.; (iii) the increase of the chain growth probability (α) suggests that type II sites (chain growth) are increasing with T.o.S.; (iv) the increase of the O/P ratio suggests that type III sites (secondary olefins hydrogenation) are decreasing with T.o.S..

Similar results have been reported by Shultz et al. [53] for CO_2 hydrogenation at temperature and pressure higher than those we used for a Fe/Al/Cu/K catalyst activated in H_2 at 400 °C for 10 h.

3.2.1.3. Steady state activity. After 75 h on stream K-Fe15 catalyst reaches steady state conditions, characterized by CO_2 conversion of about 38% and similar H_2 conversion (Figs. 8(a) and 9). Notably, lower olefins are the most abundant products, with a selectivity close to 40%, followed by C_5–C_9 olefins (21%). CH_4 selectivity is close to 19%, while that of CO is 13% (Figs. 8(b) and 10(b)). The distribution of C_1–C_9 hydrocarbons is shown in Fig. 11. Notably, the products closely follow a quasi-ideal Anderson-Schulz-Flory (ASF) distribution, with methane slightly higher than expected and C_2-species slightly lower. This well resembles what happens in the case of CO hydrogenation on Fe-based catalysts [9,10]. The linear product distribution for the C_{3+} species allows to estimate that the carbon converted to C_{10+} hydrocarbons at reference conditions (270 °C, 5 barg) is less than 10% of that converted to C_1–C_9 hydrocarbons.

Once reached steady conditions, the effects of the process variables have been investigated.

3.2.1.4. Effect of temperature. The effect of temperature has been assessed by running experiments at 270 and 300 °C (conditions #1 and #2 in Table 1). By increasing the temperature from 270 °C to 300 °C, CO_2 conversion increases from 37.6% to 45.1% and the selectivity to CO decreases from 13.1% to 12.1% (Fig. 10(a) and (b)). At the same time C_2–C_9 olefins increase while C_2–C_4 paraffins decrease (Fig. 10(b)). As a result, the olefin/paraffin ratio (Fig. 12(a)) increases with temperature. It is worth noting that RWGS is quasi-equilibrated at the adopted process conditions, as demonstrated by K_p/K_{eq} ratio (Eq. (9)):

$$\frac{K_p}{K_{eq}} = \frac{P_{CO}^{out} \cdot P_{H_2O}^{out}}{P_{H_2}^{out} \cdot P_{CO_2}^{out}} \cdot exp\left(\frac{\Delta G_{R,RWGS}^{0}(T)}{R \cdot T}\right) \quad (9)$$

This ratio is indeed 0.6 at 270 °C, and ~1 at 300 °C. As a consequence, upon increasing the temperature, H_2/CO ratio in the

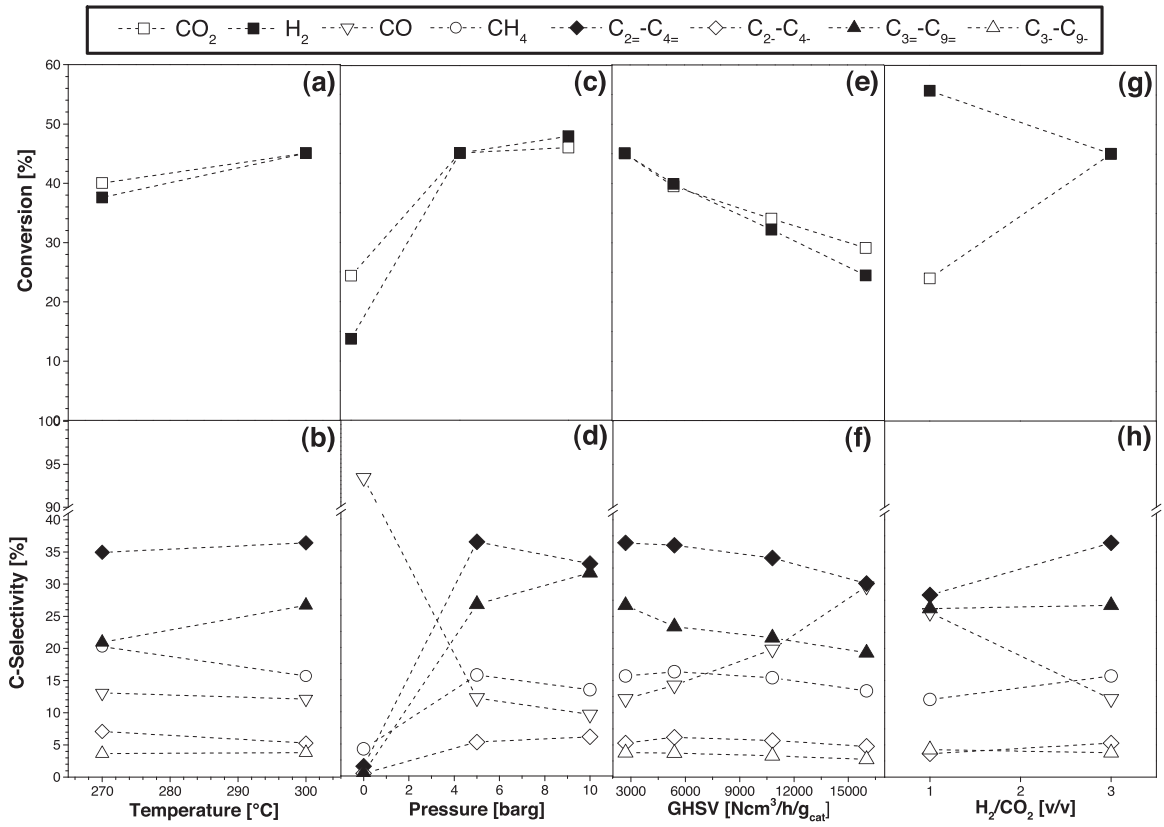

Fig. 10. Effect of (a–b) temperature, (c–d) pressure, (e–f) GHSV and (g–h) H_2/CO_2 inlet molar ratio on CO and H_2 conversions and C-selectivities for K-Fe15 catalyst. Process conditions as in Fig. 8.

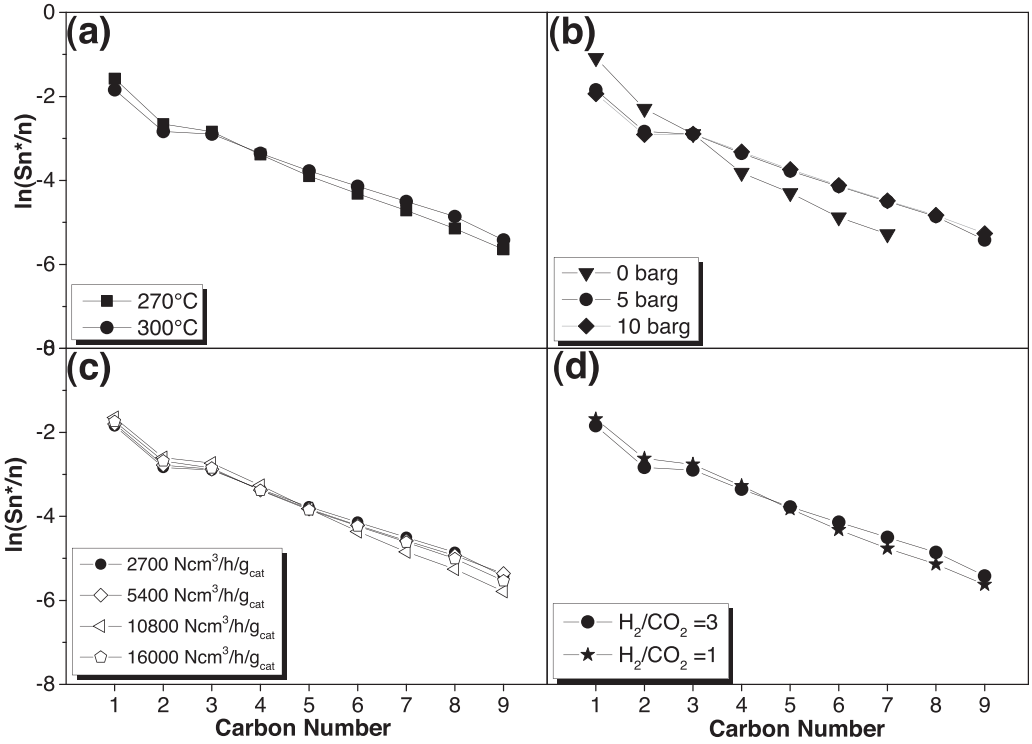

Fig. 11. Effect of (a) temperature, (b) pressure, (c) GHSV and (d) H_2/CO_2 inlet molar ratio on the C_1–C_9 hydrocarbon distribution for K-Fe15 catalyst. Process conditions as in Fig. 8. S_i* are CO-free carbon selectivities.

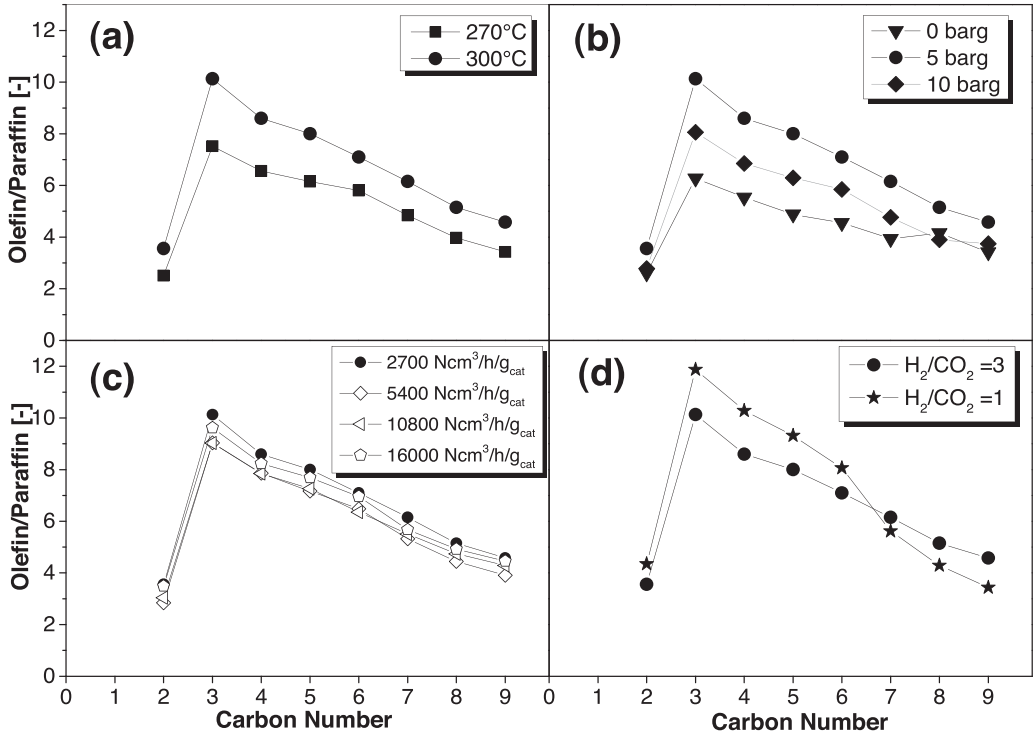

Fig. 12. Effect of (a) temperature, (b) pressure, (c) GHSV and (d) H_2/CO_2 inlet molar ratio on the Olefin/Paraffin ratio for K-Fe15 catalyst. Process conditions as in Fig. 8.

reactor decreases ($P^{out}_{H_2}/P^{out}_{CO}$ = 66 at 270 °C and 52 at 300 °C). This, in turn, results both in a slightly higher chain growth probability ($\alpha_{C3\text{-}C9}$ = 0.63 at 270 °C and 0.67 at 300 °C, see also Fig. 11(a)), in a decreased CH_4 selectivity and in a higher olefin content (and hence in increased O/P ratio).

3.2.1.5. Effect of pressure. In order to evaluate the effect of pressure on the catalytic performances, the K-Fe15 sample has been tested at 0, 5 and 10 barg (conditions #3, #2 and #4 in Table 1). As shown in Fig. 10(c), CO_2 conversion strongly increases by increasing the pressure from 0 to 5 barg. Only minor improvements in CO_2 conversion are instead observed by increasing the pressure from 5 to 10 barg.

As proved by the value of the H_2/CO_2 usage ratio, which increases from 1.5 to 3 upon increasing the pressure from 0 to 5 barg, pressure dramatically influences the product selectivity. At atmospheric pressure the selectivity to CO is close to 95% (Fig. 10(d)), which indicates a dominant RWGS regime. At the same time, the slope of the ASF plot is very high (Fig. 11(b)), indicating a very low chain growth probability ($\alpha_{C3\text{-}C7}$ = 0.56). On the contrary, by increasing the pressure, a regime dominated by the synthesis of hydrocarbons is established, with much lower CO selectivity (12% at 5 barg and 10% at 10 barg). These results point out that a pressure higher than the atmospheric is needed to effectively convert CO_2 into hydrocarbons.

Among the hydrocarbons, olefins largely dominate at 5 and 10 barg, in particular in the range C_2–C_4.

Interestingly, only minor variations are observed in terms of selectivity when increasing the pressure from 5 to 10 barg (Figs. 10 (c),(d) and 11 (b)). Accordingly, 5 barg seems a reasonable pressure to maximize the selectivity to lower olefins, minimizing complexity and costs associated to high pressure operations. Furthermore, 5 barg is the pressure maximizing the olefin/paraffin ratio (Fig. 12(b)).

3.2.1.6. Effect of space velocity. In order to evaluate the effect of the space velocity on the catalyst performances, the K-Fe15 sample has been tested at 2700, 5400, 10800, 16000 $Ncm^3/h/g_{cat}$ (conditions #2, #5, #6 and #7 in Table 1). As expected, due to the reduced contact time, CO_2 and H_2 conversions decrease almost linearly by raising the GHSV (Fig. 10(e)). At the same time, selectivities to hydrocarbon products decrease, while CO selectivity progressively increases (Fig. 10(f)).

The trend of selectivities can be used to obtain further insights on the reaction mechanism for the formation of CO and hydrocarbons from CO_2. In Fig. 13, C-selectivities to different reaction products obtained in test at different GHSV are plotted as function of CO_2 conversion. Trends are extrapolated to zero conversion. Notably, selectivities to CH_4, C_3H_6, C_3H_8, C_6H_{12}, C_6H_{14} go to zero at nil CO_2 conversion. This indicates that those species are secondary products. On the contrary, CO selectivities goes to 100%, suggesting that CO is the only primary product of the reaction. In other words, these data suggest that CO_2 is primarily converted to CO through RWGS reaction (Eq. (1)), then CO is hydrogenated to hydrocarbons (Eq. (2)). These results confirm the two-step mechanism proposed by Riedel and co-workers [61].

Fig. 12(c) shows that GHSV only slightly affects the olefin/paraffin ratio. The same conclusion can be drawn by looking at the GHSV effects on the ASF distribution (Fig. 11(c)). These results suggest that the adopted catalyst has a limited activity in the hydrogenation of olefins to the corresponding paraffins. This conclusion is in line with literature papers showing the secondary hydrogenation reactions are depressed on K-promoted Fe-based catalysts because potassium weakens H_2 adsorption [62].

3.2.1.7. Effect of H_2/CO_2 inlet ratio. Finally, the effect of the H_2/CO_2 inlet ratio has been investigated by testing the catalyst at H_2/CO_2 molar ratios of 3 and 1 (conditions #2 and #8 in Table 1). By decreasing the ratio from 3 to 1, CO_2 conversion decreases from 45% to 24% (Fig. 10(g)), CO selectivity increases from 12% to 26%, whereas both CH_4 and C_2–C_4 olefins decrease (Fig. 10(h)). Such result can be explained considering that the rate of CO hydrogenation to hydrocarbons decreases upon decreasing the H_2 content in the feed.

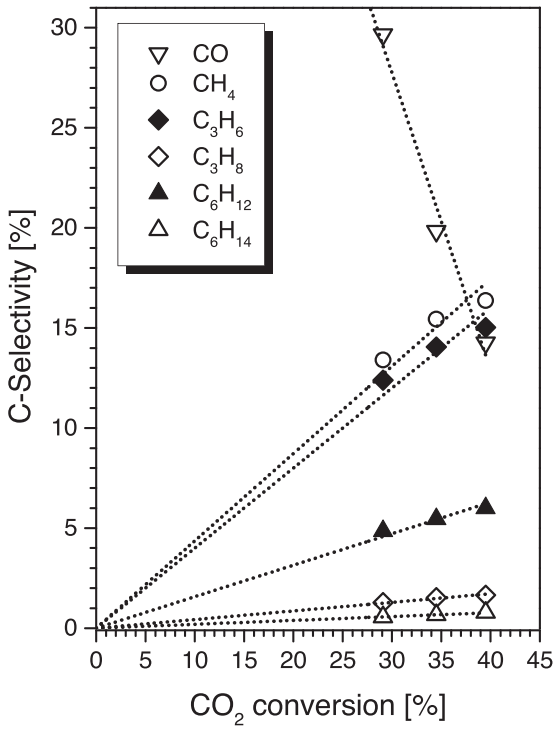

Fig. 13. C-selectivity in function of CO_2 conversion (process conditions: T = 300 °C, P = 5 barg, H_2/CO_2 = 3 v/v).

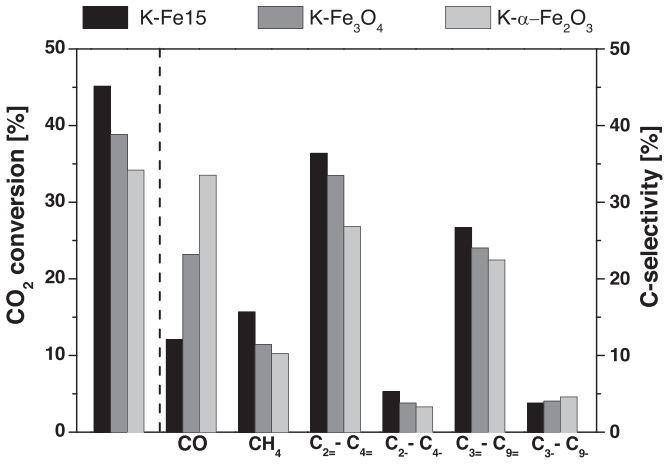

Fig. 14. CO_2 conversion and C-selectivity for K-Fe15, K-Fe_3O_4 and K-α-Fe_2O_3 samples (process conditions: T = 300 °C, P = 5 barg, H_2/CO_2 = 3 v/v and GHSV = 41 $Ncm^3/h/m^2_{cat}$).

Table 5
Reaction parameters for K-Fe15, K-α-Fe_2O_3 and K-Fe_3O_4 samples (process conditions: T = 300 °C, P = 5 barg, GHSV = 41 $Ncm^3/h/m^2_{cat}$, H_2/CO_2 = 3 v/v).

	Amount of catalyst in the reactor [g]	H_2/CO_2 molar usage ratio	α_{C3-C9}
K-Fe15	0.5	3	0.67
K-α-Fe_2O_3	5.5	2.5	0.65
K-Fe_3O_4	5.0	2.4	0.66

Not surprisingly, the decrease of the H_2/CO_2 ratio increases the olefin/paraffin ratio (Fig. 12(d)), although this effect is minor. This can be explained by considering that upon decreasing H_2/CO_2 ratio in the feed, H/C ratio on the catalyst surface is lower and thus the already slow secondary olefins reactions become even slower.

The lower CO hydrogenation rate and the lower hydrogen surface coverage are also responsible for a lower rate of formation of the chain growth monomer. This, in turn, results in a decreased chain growth probability, which is evident by looking at the ASF plot reported in Fig. 11(d).

3.2.1.8. Characterization of the used catalyst. In order to collect experimental indications on the possible dominant sites on the catalyst surface, the used K-Fe15 catalyst, operated for more than 650 h at many different process conditions, has been characterized by XRD and XPS. Notably, the characterized sample contains some α-Al_2O_3, which has been used as diluent for the catalyst bed to control the reaction exothermicity (see Section 2.3).

The XRD pattern of the used catalyst, shown in Fig. 6, clearly shows that iron carbides (possibly Hägg carbides) are present on the surface of the used catalyst, while Fe_3O_4 species are almost undetectable. In addition, no peaks corresponding to α-Fe_2O_3 or α-Fe are visible. The XPS spectrum (Fig. 2), complementary, shows that the surface is particularly rich of carbon (Table 2), which is another indication of the presence of active carbides.

These results are in good agreement with the observed reactivity of K-Fe15 catalyst, which is characterized by: (i) a low CO selectivity, which indicates that CO_2 consumption, activated by type I sites, is slow if compared to type II sites-catalysed CO consumption; (ii) a slow rate of secondary olefin reactions, activated by type III sites, which results in a low selectivity to oxygenated hydrocarbons and in a high O/P ratio.

3.2.2. K-promoted a-Fe_2O_3 and Fe_3O_4 reference samples

3.2.2.1. Catalyst activation. The specific flow rates (per unit of catalyst surface area) of CO, H_2, CH_4 and CO_2 measured during the activation process of K-α-Fe_2O_3 and K-Fe_3O_4 samples are reported as a function of time in Fig. 7(b) and (c), respectively.

For the K-α-Fe_2O_3 sample, the production of some CO_2 is observed in the temperature range 120–170 °C, possibly due to the decomposition of some residual carbonates on the catalyst surface (Fig. 7(b)). No CO consumption is observed until a temperature of 245 °C, then CO flow rate starts to decrease and monotonically continues until the heating ramp is stopped at 350 °C. The CO consumption results in a corresponding CO_2 formation, but no H_2 consumption is observed until a temperature of 330 °C. This suggests that in the 245–330 °C temperature range Fe_2O_3 is reduced by CO to Fe_3O_4 (Eq. (10)) and/or to metal iron (Eq. (11)):

$$3Fe_2O_3 + CO \rightarrow 2Fe_3O_4 + CO_2 \quad (10)$$

$$Fe_3O_4 + 4CO \rightarrow 3Fe^0 + 4CO_2 \quad (11)$$

At temperatures higher than 330 °C, the CO_2 release does not correspond to CO consumption and also H_2 is consumed. This is likely associated to carbon deposition, accordingly to stoichiometries of reactions Eq. (7) and Eq. (8). As previously discussed, the formation of some CH_4 confirms that some iron carbides are formed at these conditions.

The behaviour of K-Fe_3O_4, shown in Fig. 7(c), is different. In addition to the small peak in CO_2 profile observed at about 150 °C and associated to the decomposition of residual carbonates, two main peaks are detected in CO_2 and CO profiles. The first peak occurs between 190 °C and 300 °C and is not associated with carbon deposition. Accordingly, as in the case of K-α-Fe_2O_3, this peak is due to the reduction of Fe_2O_3 impurity contained in the sample to Fe_3O_4 (Eq. (10)). The second peak, seen above 300 °C together with H_2 consumption, is associated to some carbon deposition and to the formation of iron carbides. As consequence of the formation of these latter species, CH_4 is formed at temperatures over 340 °C.

Notably, in the activation of all investigated iron based catalysts, carbon deposition and carbides formation occur only when

the catalysts are at least partially reduced. However, on K-α-Fe_2O_3 and K-Fe_3O_4 samples, the reduction, the deposition of carbon and the formation of methane are shifted at higher temperature than with K-Fe15 sample. The reference samples are also characterized by a formation of methane, which is slower than on home-made catalyst. These results suggest a higher "extent of activation" for the K-Fe15 sample. This can be explained considering that the less densely packed structure, obtained by the thermal decomposition of iron glycolate complexes, improves the reduction of the small Fe_3O_4 crystallites to Fe^0 [35] and consequently their carburation to iron carbides.

3.2.2.2. Steady state activity. The catalytic performances in CO_2 hydrogenation of the reference model catalysts have been evaluated and compared to those of K-Fe15 sample at the same T, P, H_2/CO_2 inlet ratio and reactants flowrate per unit of catalyst surface area. The main results are shown in Fig. 14 and Table 5. In terms of activity, K-Fe15 shows the highest CO_2 conversion, while the K-α-Fe_2O_3 catalyst has the lowest CO_2 conversion. K-Fe15 catalyst has also the highest selectivity to lower olefins and the lowest CO selectivity. Again the catalytic system with the worst performances is K-α-Fe_2O_3, which shows a high CO selectivity (over 30%) and a low olefins selectivity.

We attribute the highest activity and C_2–C_4 olefins selectivity of K-Fe15 catalyst to its textual, morphological and crystalline properties, which result in the better carburization of iron centers and thus in the maximization of type II sites (CO activation and chain growth) compared with type I sites (WGS/RWGS sites). These results further indicate that both RWGS (Eq. (1)) and the consecutive synthesis of hydrocarbons from CO (Eq. (2)) are taking place on the catalyst.

4. Conclusion

A bulk iron catalyst with high surface area (67 m^2/g) has been prepared by thermal decomposition of ammonium glycolate complexes, without adding any structural promoter or other heteroatoms. We have found that a careful control of the calcination process allows to achieve high surface area and avoids the transformation of the spinel structure (Fe_3O_4/γ-Fe_2O_3) into the more stable corundum structure of α-Fe_2O_3. The catalyst with a spinel structure, activated with syngas at 350 °C, has been found to be active in CO_2 hydrogenation, with lower olefins (C_2–C_4) being the most abundant species in the products pool at 300 °C, 5 barg, H_2/CO_2 inlet ratio = 3, GHSV = 2700 $Ncm^3/h/g_{cat}$.

The analysis of the effect of the process conditions has shown that by optimizing the pressure and increasing the temperature it is possible to boost both CO_2 conversion and the olefin/paraffin ratio. The optimal pressure is 5 barg because at this condition the synthesis of hydrocarbon from CO is favoured and the olefin/paraffin ratio reaches the highest value. By increasing the GHSV, CO_2 conversion get worse since the contact time decreases and at the same time CO selectivity rises. These data are in line with a reaction mechanism involving CO as the primary product of CO_2 hydrogenation, and hydrocarbons being formed via CO hydrogenation following a Fischer-Tropsch type (polymerization) mechanism. This results in a product distribution which closely follows the ideal Anderson-Schulz-Flory plot, with only methane and ethylene slightly out of trend.

The prepared catalyst shows better performances than two reference model samples (K-α-Fe_2O_3 and K-Fe_3O_4) in CO_2 hydrogenation. This is ascribed to its higher surface area and spinel structure that facilitate its reduction and carburization. In turn this results in a better catalytic activity because of the maximization of type II sites (active in CO activation and C–C bond formation) compared to type I sites (active in WGS/RWGS process).

Acknowledgements

XPS and TEM analyses have been performed within the Spanish Project CTQ2015-68951-C3-3R (Ministerio de Economía y Competitividad, Spain and FEDER Funds), which we acknowledge for the support.

References

[1] S. Saeidi, N.A.S. Amin, M.R. Rahimpour, J. CO_2 Util. 5 (2014) 66–81.
[2] W. Wang, S. Wang, X. Ma, J. Gong, Chem. Soc. Rev. 40 (2011) 3703–3727.
[3] G. Centi, S. Perathoner, Catal. Today 148 (2009) 191–205.
[4] I. Omae, Catal. Today 115 (2006) 33–52.
[5] G. Centi, G. Iaquaniello, S. Perathoner, ChemSusChem 4 (2011) 1265–1273.
[6] E.A. Quadrelli, G. Centi, ChemSusChem 4 (2011) 1179–1181.
[7] C. Song, Catal. Today 115 (2006) 2–32.
[8] C.G. Visconti, L. Lietti, E. Tronconi, P. Forzatti, R. Zennaro, E. Finocchio, Appl. Catal. A: Gen. 355 (2009) 61–68.
[9] M. Martinelli, C.G. Visconti, L. Lietti, P. Forzatti, C. Bassano, P. Deiana, Catal. Today 228 (2014) 77–88.
[10] C.G. Visconti, M. Martinelli, L. Falbo, L. Fratalocchi, L. Lietti, Catal. Today http://dx.doi.org/10.1016/j.cattod.2016.04.010.
[11] Y. Yao, X. Liu, D. Hildebrandt, D. Glasser, Ind. Eng. Chem. Res. 50 (2011) 11002–11012.
[12] H.M. Torres Galvis, K.P. de Jong, ACS Catal. 3 (2013) 2130–2149.
[13] A.H. Tullo, Chem. Eng. News 81 (2003) 15–16.
[14] T. Xu, Q. Zhang, H. Song, Y. Wang, J. Catal. 295 (2012) 232–241.
[15] S.H. Kang, J.W. Bae, K.J. Woo, P.S.S. Prasad, K.W. Jun, Fuel Process. Technol. 91 (2010) 399–403.
[16] H.M. Torres Galvis, A.C.J. Koeken, J.H. Bitter, T. Davidian, M. Ruitenbeek, A.I. Dugulan, K.P. de Jong, J. Catal. 303 (2013) 22–30.
[17] B. Hu, S. Frueh, H.F. Garces, L. Zhang, M. Aindow, C. Brooks, E. Kreidler, S.L. Suib, Appl. Catal. B: Environ. 132–133 (2013) 54–61.
[18] H.M. Torres Galvis, J.H. Bitter, C.B. Khare, M. Ruitenbeek, A.I. Dugulan, K.P. de Jong, Science 335 (2012) 835–838.
[19] D. Chen, K. Moljord, A. Holmen, Micropor. Mesopor. Mater. 164 (2012) 239–250.
[20] T. Zhao, T. Takemodo, N. Tsubaki, Catal. Commun. 7 (2006) 647–650.
[21] J. Wei, J. Sun, Z. Weng, C. Fang, Q. Ge, H. Xu, Catal. Sci. Technol. 6 (2016) 4786–4793.
[22] J. Wang, Z. You, Q. Zhang, W. Deng, Y. Wang, Catal. Today 215 (2013) 186–193.
[23] Z. You, W. Deng, Q. Zhang, Y. Wang, Chin. J. Catal. 34 (2013) 956–963.
[24] H. Kim, D.H. Choi, S.S. Nam, M.J. Choi, K.W. Lee, Stud. Surf. Sci. Catal. 114 (1998) 407–410.
[25] R. Satthawong, N. Koizumi, C. Song, P. Prasassarakich, Catal. Today 251 (2015) 34–40.
[26] J. Zhang, S. Lu, X. Su, S. Fan, Q. Ma, T. Zhao, J. CO_2 Util. 12 (2015) 95–100.
[27] R.E. Owen, J.P. O'Byrne, D. Mattia, P. Plucinski, S.I. Pascu, M.D. Jones, ChemPlusChem 78 (2013) 1536–1544.
[28] R.A. Fiato, E. Iglesia, G.W. Rice, S.L. Soled, Stud. Surf. Sci. Catal. 114 (1998) 339–344.
[29] Q. Zhang, J. Kang, Y. Wang, ChemCatChem 2 (2010) 1030–1058.
[30] G. Van Laan, A. Beenackers, Catal. Rev. Sci. Eng. 41 (1999) 255–318.
[31] D.G. Miller, M. Moskovits, J. Phys. Chem. 92 (1988) 6081–6085.
[32] D. Mattia, M.D. Jones, J.P. O'Byrne, O.G. Griffiths, R.E. Owen, E. Sackville, M. McManus, P. Plucinski, ChemSusChem 8 (2015) 4064–4072.
[33] L. Xu, Q. Wang, D. Liang, X. Wang, L. Lin, W. Cui, Y. Xu, Appl. Catal A: Gen. 173 (1998) 19–25.
[34] Patent US 5,140,049 assigned to Exxon Research and Engineering Co. (1992).
[35] S.L. Soled, E. Iglesia, S. Miseo, B. DeRites, R. Fiato, Top. Catal. 2 (1995) 193–205.
[36] J.B. Bialecky, F.U. Axe, A.B. Attygalle, J. Mass Spectrom. 44 (2009) 252–259.
[37] K. KoJima, M. Miyazaki, J. Sol-Gel Sci Tech. 8 (1997) 77–81.
[38] M. Stefanescu, O. Stefanescu, M. Stoia, C. Lazau, J. Therm. Anal. Calorim. 88 (2007) 27–32.
[39] E. Bermejo, R. Carballo, A. Castineiras, A.B. Lago, Coord. Chem. Rev. 257 (2013) 2639–2651.
[40] M. Omrana, T. Fabritius, A.M. Elmahdy, N.A. Abdel-Khalek, M. El-Aref, A.E.H. Elmanawi, App. Surf. Sci. 345 (2015) 127–140.
[41] S.J. Roosendaal, B. van Asselen, J.W. Elsenaar, A.M. Vredenberg, F.H.P.M. Habraken, Surf. Sci. 442 (1999) 329–337.
[42] P. Grosvenor, B.A. Kobe, M.C. Biesinger, N.S. McIntyre, Surf. Interface Anal. 36 (2004) 1564–1574.
[43] H. Wan, B. Wu, C. Zhang, H. Xiang, Y. Li, J. Mol. Catal. A: Chem. 283 (2008) 33–42.
[44] A.A. Mirzaei, R. Habibpour, M. Faizi, E. Kashi, App. Catal. A: Gen. 301 (2006) 272–283.
[45] Z. Tao, Y. Yang, C. Zhang, T. Li, M. Ding, H. Xiang, Y. Li, J. Nat, Gas Chem. 16 (2007) 278–285.
[46] M.K. Gnanamani, H.H. Hamdeh, G. Jacobs, W.D. Shafer, D.E. Sparks, B.H. Davis, Fischer-Tropsch Synthesis, Catalysts, and Catalysis: Advances and Applications, CRC Press, 2016.
[47] S. Soled, E. Iglesia, R.A. Fiato, Catal. Lett. 7 (1990) 271–280.

[48] W. Kim, C.Y. Suh, S.W. Cho, K.M. Roh, H. Kwon, K. Song, I.J. Shon, Talanta 94 (2012) 348–352.
[49] Y.E. Mendili, J.F. Bardeu, N. Randrianantoandro, F. Grasset, J.M. Greneche, J. Phys. Chem. C 116 (2012) 23785–23792.
[50] N. Lohitharn, J.G. Goodwin, J. Catal. 260 (2008) 7–16.
[51] G. Munteanu, L. Ilieva, D. Andreeva, Thermochim. Acta 291 (1997) 171–177.
[52] W.K. Jozwiak, E. Kaczmarek, T.P. Maniecky, M. Ignaczak, W. Maniukiewicz, Appl. Catal. A: Gen. 326 (2007) 17–27.
[53] H. Schulz, G. Schaub, M. Claeys, T. Riedel, Appl. Catal. A: Gen. 186 (1999) 215–227.
[54] R.J. O'Brien, L. Xu, L. Spicer, S. Bao, D.R. Milburn, B.H. Davis, Catal. Today 325 (1997) 325–334.
[55] H. Schulz, Catal. Today 228 (2014) 113–122.
[56] T. Riedel, H. Schulz, G. Schaub, K.W. Jun, J.-S. Hwang, K.W. Lee, Top. Catal. 26 (2003) 41–54.
[57] E. de Smit, B. Weckhuysen, Chem. Soc. Rev. 37 (2008) 2758–2781.
[58] H.B. Zhang, G.L. Schrader, J. Catal. 95 (1985) 325–332.
[59] M.K. Gnanamani, G. Jacobs, H.H. Hamdeh, W.D. Shafer, B.H. Davis, Catal. Today 207 (2013) 50–56.
[60] H. Schulz, T. Riedel, G. Schaub, Top. Catal. 32 (2005) 117–124.
[61] T. Riedel, G. Schaub, K.W. Jun, K.W. Lee, Ind. Eng. Chem. Res. 40 (2001) 1355–1363.
[62] D.B. Bukur, D. Mukesh, S.A. Patel, Ind. Eng. Chem. Res. 29 (1990) 194–204.